Nickel-free SOFC anode for ethanol electrocatalysis

Sarruf, Bernardo; Coralli, Alberto; Hong, Jong-Eun; Steinberger-Wilckens, Robert; de Miranda, Paulo Emilio V.

DOI:
10.1149/09101.1673ecst

ECS Transactions, 91 (1) 1673-1682 (2019)
10.1149/09101.1673ecst ©The Electrochemical Society

Nickel-free SOFC Anode for Ethanol Electrocatalysis

B. J. M. Sarruf[a], A. Coralli[a], J-E. Hong[b], R. Steinberger-Wilckens[c] and P. E. V. de Miranda[a]

[a] Hydrogen Laboratory COPPE, Federal University of Rio de Janeiro, Brazil
[b] Fuel Cell Laboratory, Korea Institute of Energy Research, South Korea
[c] Centre for Fuel Cell and Hydrogen Research, University of Birmingham, UK

In this paper the development of an anode material capable of electro-oxidising primary fuels in an SOFC is proposed. Due to the issues presented by nickel-based anodes regarding direct utilisation of carbon-rich fuels, that have been well-scrutinised within the literature, a ceria-Co-Cu-based anode development has been the target of this work. X-ray patterns for the electrocatalyst powder show the presence of ceria and cobalt oxide, whereas for the anode surface, they unveil the formation of ceria, cobalt and impregnated copper upon reduction. Temperature-programmed reduction of the ceria-Co powder showed the ability of cobalt oxide to fully reduce and the partial reduction of ceria, as expected, leaving an oxygen-deficient lattice. The nickel-free material has shown the ability to operate as an SOFC anode with carbonaceous fuels and hydrogen. The microstructural phase distribution was assessed aided by scanning electron microscopy and energy dispersive X-ray spectroscopy.

Introduction

Solid oxide fuel cells (SOFC) are a constantly progressing technology that has been a protagonist in the emerging zero-carbon era. Efforts are being made to overcome the issues related with bulk hydrogen production and distribution infrastructure issues. One promising solution is the direct utilisation of zero-net carbon fuels such as ethanol, biogas or synthetic methane (1).

Considering hydrogen cost of 3 US$/kg against 0.5 US$/kg of that of ethanol's (Brazilian market), the direct utilisation of these primary fuels can lower the cost of fuel by a factor of 6, when compared to pure hydrogen. Taking into account fuel high heating values (39.4 and 8.3 kWh/kg for hydrogen and ethanol, respectively) this represents around 25% reduction in OPEX (US$/kWh).

Therefore, research worldwide has been concentrating on direct carbonaceous fuel utilisation in SOFC (2-6). and Success has mostly depended on materials development, specially focused on preventing carbon deposition and subsequent cell deactivation. Furthermore, anode developers have dedicated themselves to the study of nickel-free anode materials, since it is well-known, that nickel is the main responsible for catalysing carbon formation reactions such as methane cracking or the Boudouard reaction, which subsequently deteriorates the SOFC anode function. Our group have been investigating

new materials for ethanol and methane direct utilisation within an SOFC since 2008 (7, 8, 9).

The ethanol dehydrogenation takes place following the elementary steps represented by the reactions shown in Equations 1 to 7. It is a process that inevitably leaves carbon as product throughout the anode tortuous porosity accessible surface. The main difference between an adequate catalyst for ethanol utilisation and a coking-prone one is the ability the former presents to facilitate carbon oxidation post adhesion to the catalyst surface (Equations 8-10), in the present case of an SOFC anode, by oxygen ions.

$$C_2H_5OH + 2* \rightarrow C_2H_5* + OH^-* \quad [1]$$

$$C_2H_5* + 2* \rightarrow CH_3* + CH_2* \quad [2]$$

$$CH_3* + 2* \rightarrow CH_2* + H^+* \quad [3]$$

$$CH_2* + H^+* + OH^-* \rightarrow CH_2* + H_2O \quad [4]$$

$$2CH_2* + 2* \rightarrow 2CH* + 2H^+* \quad [5]$$

$$2CH* + 2H^+* + O^{2-} \rightarrow 2CH* + H_2O + 2e^- \quad [6]$$

$$2CH* + 2* \rightarrow 2C* + 2H^+* \quad [7]$$

$$2C* + 2H^+* + O^{2-} \rightarrow 2C* + H_2O + 2e^- \quad [8]$$

$$2C* + 2O^{2-} \rightarrow 2CO* + 4e^- \quad [9]$$

$$2CO* + 2O^{2-} \rightarrow 2CO_2 + 4e^- \quad [10]$$

The described process can be simplified by the full electrochemical oxidation of ethanol in Equation 11.

$$C_2H_5OH + 6O^{2-} \rightarrow 2CO_2 + 3H_2O + 12e^- \quad [11]$$

Ceria-based materials have been successfully used for that purpose since its non-stoichiometric fluorite structure serves as an oxygen buffer capable of storing and releasing the oxygen ions permeating through the electrolyte (9). In addition to this, the associations with transition metals, such as cobalt, have shown to enhance catalytic activity for ethanol adsorption. However, since cobalt is a transition metal of the *d* family, such as nickel, it has been proven to favour hydrocarbon cracking, especially when the SOFC cell is operating at Open Circuit Voltage (OCV), thus in thermodynamical equilibrium when oxygen ions are not abundantly present. For this reason, copper additions have been used to facilitate carbon release upon oxygen ion presence. In Sarruf et al. (10), the ceria-Co-Cu cell was able to operate with direct ethanol delivering more than 400 $mW.cm^{-2}$ at 850˚C.

Given the background offered, this work aims at developing a nickel-free anode electrocatalyst in which the flow of oxygen ions could be facilitated, and electrochemical

oxidation of directly-fed ethanol could take place. The authors in the following describe the development and production as well as the preliminary results of a Co-Cu-ceria-based anode within an electrolyte-supported SOFC cell that was operated with direct utilisation of unreformed ethanol.

Experimental

The ceria-Co_3O_4 electrocatalyst powder was produced by the mixing oxides method. Ceria and Co_3O_4 were mixed in a molar proportion of 1:3 (Ce:Co) aided by high energy planetary milling for 5 hours at 250 rpm. Subsequently, 30 vol. % of potato starch (Sigma-Aldrich) was added to the powder mixture to serve as pore former.

Additionally, a ceria-based suspension was prepared to serve as anode buffer layer, aiming at alleviating the thermal expansion mismatch between the metallic anode upon reduction and the ceramic electrolyte. The CeO_2 powder was mixed with 10Sc1CeSZ electrolyte powder in a weight proportion of 1:1 and 20 wt. % of potato starch was added to the mixture. The buffer layer suspension was screen printed onto 150 µm thick ScCeSZ-Hionic® electrolyte buttons (Fuel Cell Materials) and sintered at 1300˚C for 3 hours. The details of this operation can be found in (9).

The cathode suspension was produced by mixing lanthanum strontium-doped manganite (20LSM, Fuel Cell Materials) with potato starch as pore former aided by a terpineol-based vehicle. The cathode ink was printed onto the other side of the electrolyte button and sintered at 1100˚C for 2 hours. The ceria-Co_3O_4-Starch (40-55-5 wt. %) anode suspension was deposited, by screen printing, over the prior buffer anode layer.

The anode layer was then sintered at 1000˚C under reducing atmosphere (5 vol. % H_2 in balanced Ar) for 3 hours. Finally, copper was added to the anode by the wet impregnation method. The aqueous impregnation solution was composed by copper nitrate and urea as precipitant agent. After each impregnation step followed by drying at 450˚C for 2 hours, each ensemble was weighed. The decision to stop the process was taken after 5 impregnation steps, which was enough to attain 50 wt. % of CuO (or 40 wt.% Cu) of the total anode mass. To complete the cell assemblies for testing, silver current collectors were added.

In order to prove that the ceria-Co_3O_4 was well mixed, X-ray diffraction (XRD) patterns of the CeO_2, Co_3O_4, and the ceria-Co_3O_4 mixture were taken. The XRD patterns were recorded from 10 to 90˚ at a continuous scanning rate of 2 ˚/min within 0.02˚ steps in a Shimadzu 6000 X-ray equipment. Temperature-programmed reduction (TPR) was performed in a Quantachrome ChemBET Pulsar TPR/TPD over the abovementioned from room temperature to 800˚C within 5 ˚C/min steps to assess the catalyst ability to reduce.

The cells were electrochemically tested by recording i-V plots, with a measuring rate of 50 mV from 700 to 825˚C first with hydrogen, then with direct ethanol. The ethanol set-up test consisted in evaporating ethanol aided by a thermostatic bath and carrying ethanol vapour with a carrier gas flow (nitrogen at ~100 mL.min-1). An SOFC cell replica was aged in a tubular furnace in H_2 5 vol. % balanced Ar at 750˚C for 50 hours. After ageing, the cell microstructure was inspected by scanning electron microscopy

(SEM), energy-dispersive X-ray spectroscopy (EDX) and X-ray analysis (with the same conditions mentioned above).

Results and Discussion

Electrocatalyst Characterisation

The precursors of the electrocatalyst were first characterised individually. The X-ray pattern for the CeO_2, Co_3O_4, and the Co_3O_4-CeO_2 mixture is presented in Figure 1. The patterns of the individual oxides were used to assure the precursor conformity. As expected per PDF-03-065-2975 (ICDD, 2016) for the Fm-3m cubic fluorite structure of CeO_2, 9 well-defined sharp peaks can be seen in Figure 1 (11).

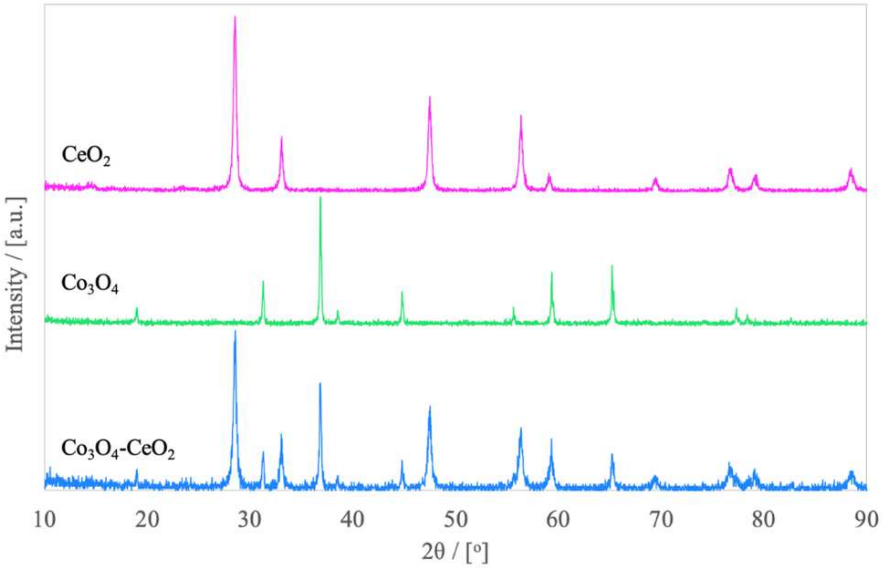

Figure 1. X-ray diffraction patterns for the isolated oxides CeO_2 and Co_3O_4 and the mixed oxides CeO_2-Co_3O_4.

The same is proven for the Co_3O_4 spinel structure that presented 10 peaks in conformity with PDF-00-042-1467 (ICDD, 2016) (12). Concerning the powder mixture, 15 peaks were well defined. However, three hidden peaks of Co_3O_4 can be noted due to a higher diffraction intensity of ceria at 56.8, 77.9 and 79.5˚. One peak of ceria is lowered by Co_3O_4 at 59.3˚. For the X-ray pattern presented for the mixture, it can be said that due to the good definition of the peaks, the high energy milling process served its purpose of homogenising the oxides. Additionally, the sharpness of the peaks indicates satisfactory phase crystallisation.

Analogously to the X-ray analysis, the temperature-programmed reduction (TPR) was performed separately over each precursor and then over the mixture. The results of TPR are shown in Figure 2. Qualitatively, it is evident that CeO_2 as a strong oxide has not undergone full reduction. As a consequence, at high temperatures (near 800˚C), a minor hydrogen consumption is noted. This confirms that ceria is partially reduced, revealing its oxygen-deficient lattice according to Equation 12.

$$CeO_2 + \delta H_2 \rightarrow CeO_{2-\delta} + \delta H_2O \quad [12]$$

Quantitatively, hydrogen consumption for the CeO_2 TPR profile was around 8.57×10^{-3} mL of H_2 per catalyst gram or 3.83×10^{-7} mols of H_2/g. Considering that 1 g of CeO_2 has around 0.012 mols of atomic oxygen, the small consumption indicates a slightly oxygen-deficient lattice (~0.007%), $CeO_{1.99}$.

Regarding cobalt oxide reduction as per Equations 13 and 14, the total hydrogen consumption was estimated as being 146.58×10^{-3} and 84.11×10^{-3} mL of H_2 per gram of catalyst for the precursor Co_3O_4 and the CeO_2-Co_3O_4 mixture, respectively. Smaller hydrogen consumption for the latter is due to its lower Co_3O_4 mass proportion.

$$Co_3O_4 + H_2 \rightarrow 3CoO + H_2O \quad [13]$$

$$CoO + H_2 \rightarrow Co + H_2O \quad [14]$$

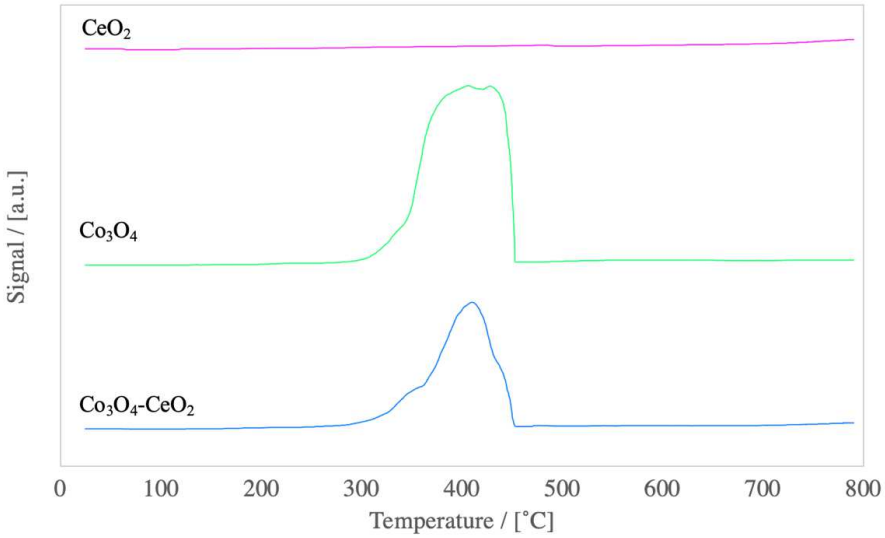

Figure 2. H_2-Temperature programmed reduction (TPR) profiles for CeO_2, Co_3O_4, and the mixed oxides CeO_2-Co_3O_4.

Cell Characterisation

A complete cell with copper added by impregnation has undergone reduction and ageing, so that X-ray analysis could be performed over the anode surface to check for superficial copper. The X-ray pattern is shown in Figure 3. The peaks assigned to ceria are again a total of 9. The cobalt oxide phase has been reduced to metallic cobalt, which is denoted by 5 well-defined peaks. Finally, copper markedly appears in the surface. This analysis was important to prove that the metallic copper has remained on the anode surface even after ageing at 750˚C for over 50 hours.

After a full cell was assembled comprising a ScCeSZr electrolyte support, LSM cathode, ceria-based anode buffer layer, ceria-Co screen-printed anode layer, and Cu added by wet impregnation, silver current collectors were pasted onto the electrode, allowing the electrochemical tests to be performed. The recorded i-V plots are shown in Figure 4. Figure 4a shows the tests with 50 $mL.min^{-1}$ dry hydrogen and 130 $mL.min^{-1}$

synthetic air, as fuel and oxidiser, respectively, at 700, 725, 750 and 775˚C. Figure 4b depicts the tests done with direct ethanol as fuel stream.

The tests with hydrogen served to attest the SOFC cell conformity with standard SOFC performance. The maximum power densities in this case were 126, 185, 254 and 300 mW.cm^{-2} corresponding to temperatures from 700 to 775˚C, respectively. Additionally, the OCVs for the different temperature values were 1.05, 1.04, 1.03 and 1.02 V, indicating an expected behaviour for a well-sealed cell with thermodynamic consistence.

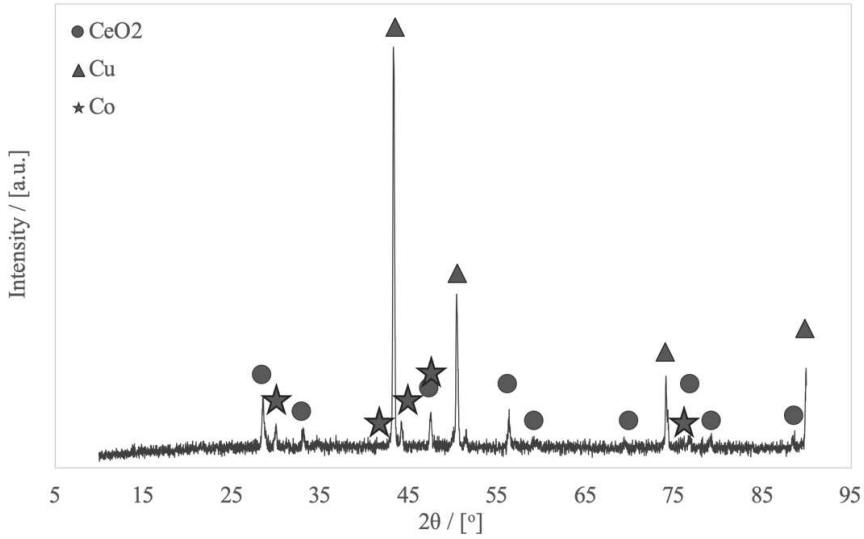

Figure 3. X-ray pattern for the SOFC cell surface after reduction in hydrogen at 750˚C for over 50h.

When the fuel stream was switched to ethanol, the i-V plots were recorded at higher temperatures such as 750, 775, 800 and 825˚C, to favour ethanol's oxidation kinetics. Figure 4b reports maximum power densities of 26, 38, 58 and 86 mW.cm^{-2} from the lower to the higher temperature.

The OCVs for the ethanol case were slightly lower: 0.96, 0.97, 0.98 and 0.99 V from 750 to 825˚C, respectively. The increase in OCV with temperature when direct ethanol is used, is explained by locally dependent changes in potential due to various reactions occurring simultaneously, a situation very different from hydrogen being primarily oxidised generating steam, as discussed in previous work (9, 10). The electrochemical results are summarised in Table I.

TABLE I. Results from i-V plots compiled for both fuel streams.

Temperature [˚C]	Hydrogen		Ethanol	
	Max P. Density [mW.cm^{-2}]	OCV [V]	Max P. Density [mW.cm^{-2}]	OCV [V]
700	126	1.05	---	---
725	185	1.04	---	---
750	254	1.03	26	0.96
775	300	1.02	38	0.97
800	---	---	58	0.98
825	---	---	86	0.99

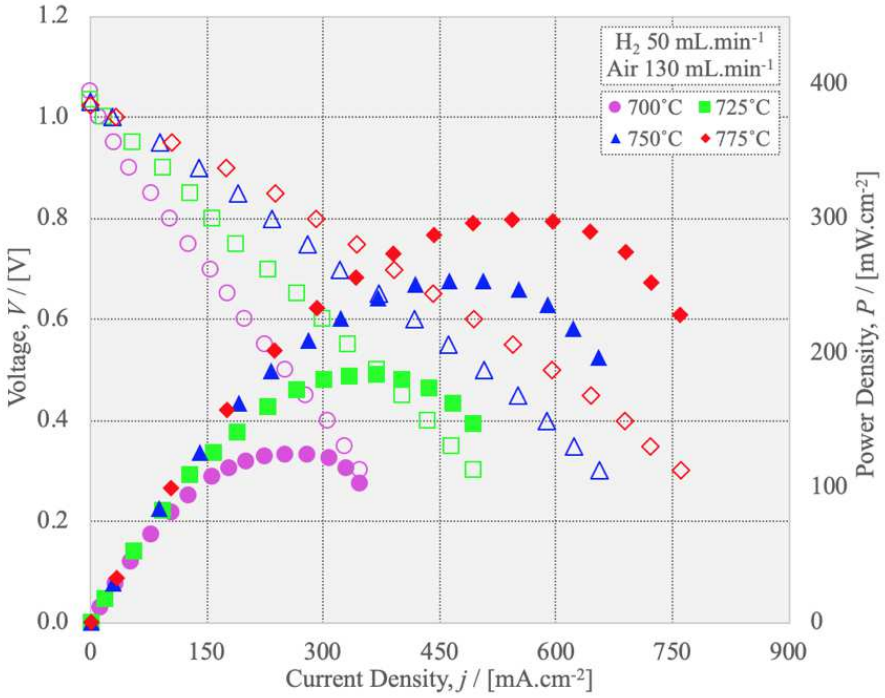

(a)

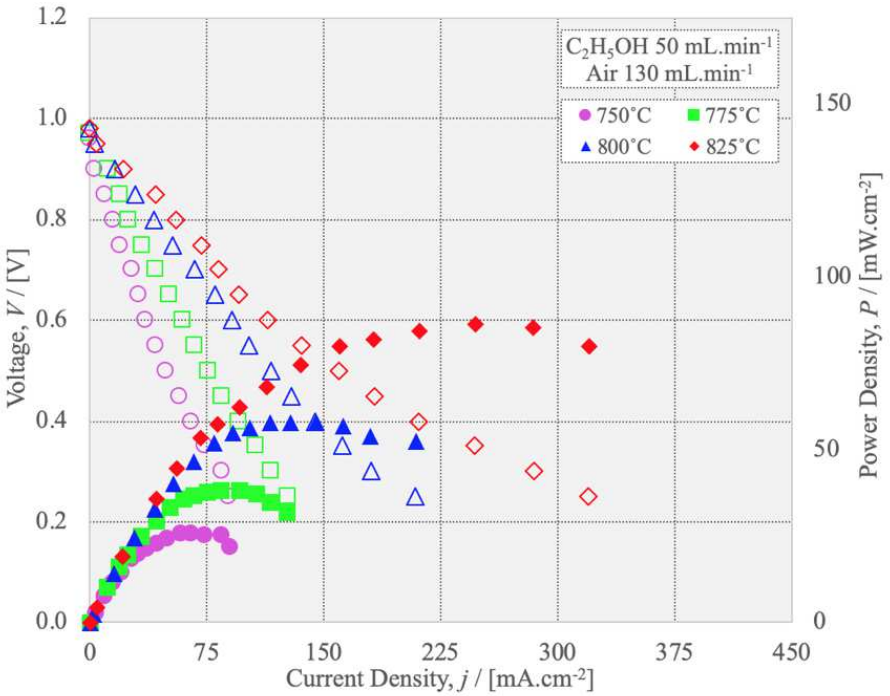

(b)

Figure 4. Electrochemical i-V plots at various temperatures with (a) hydrogen and (b) direct unreformed ethanol as fuels.

More than three different temperatures were used to record the i-V plots in order to have data for a thermal analysis. Using the results from the various temperatures, the total polarisation of the cell using each fuel was roughly estimated by Ohm's law. The Arrhenius plot for both conditions – hydrogen and ethanol as fuels – is depicted in Figure

5. Cell polarisation was then used to estimate cell Area Surface Resistance (ASR) as a matter of comparison for each fuel used.

Since the ohmic polarisation effect as a function of temperature is the same between the two cases, owing to the fact that it is mainly governed by the electrolyte in an electrolyte supported SOFC cell, it is possible to conclude that the differences between the two conditions are mostly due to fuel processing within the cell. Ethanol processing and direct utilisation is evidently delayed in respect to that of hydrogen. This statement is confirmed by the higher slope – that is by definition the activation energy – when ethanol (1.64 eV) is being directly fed, rather than hydrogen (1.05 eV).

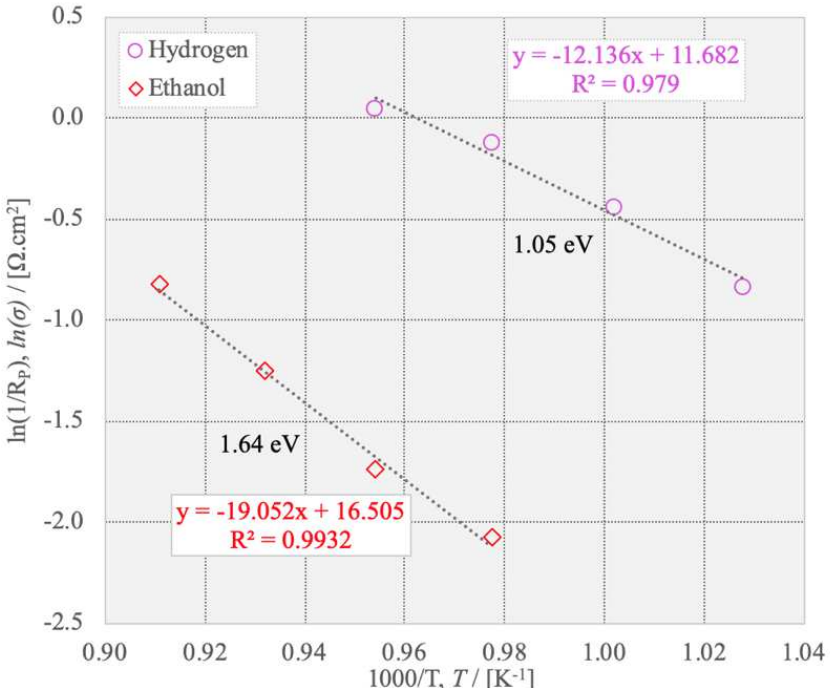

Figure 5. Arrhenius plot for the inverse of the total polarisation of the cell for tests with hydrogen and ethanol as fuels.

Figure 6 shows the anode microstructure that was reduced and aged at 750˚C for 50 hours in a hydrogen-rich atmosphere, similarly, as described in the beginning of the present section for the X-ray analysis. The microstructure shown in Figure 6 reveals the buffer layer next to the electrolyte approximately 20 μm thick, and right adjacent to it, lies the anode catalytic layer with approximately 50 μm of thickness.

Observing the microstructure, porosity looks qualitatively low compared to a conventional SOFC anode. The energy-dispersive X-ray spectroscopy (EDX) shown in the insert, reveals the phase distribution throughout the anode catalytic layer. It is evident that even though cobalt (shown in red) looks homogeneously distributed, copper (in blue) is highly concentrated on the anode surface. This concentration will naturally enhance the connection between anode surface and current collector, though a heterogenous copper distribution is not effective against carbon deposition.

A *post-mortem* cell picture is shown in Figures 7a and 7b. These images reveal that the anode was dethatched from the electrolyte, showing typical anode destruction upon

massive carbon impregnation. This drastic result corroborates with our previous work (3, 8, 9) that showed the important role played by copper in preventing coke formation.

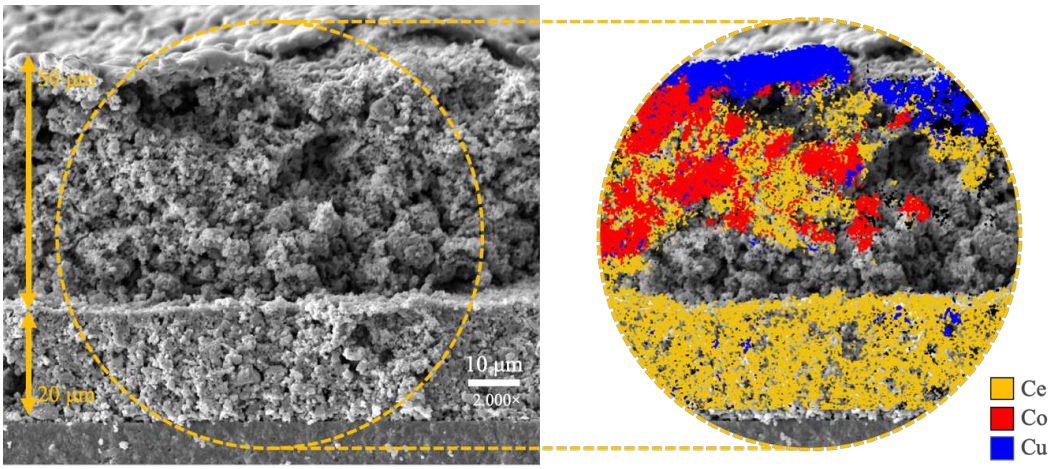

Figure 6. Scanning electron microscopy of the anode cross section showing phases distribution, with cerium in yellow, cobalt in red and copper in blue.

These results confirm the importance of copper being properly distributed in the anode. Copper decreases cobalt activity for coking and facilitates carbon post-oxidation in case of cracking. Carbon formation, observed in Figure 7, is a consequence of what is observed in the microstructure of Figure 6 – copper agglomeration over the anode surface.

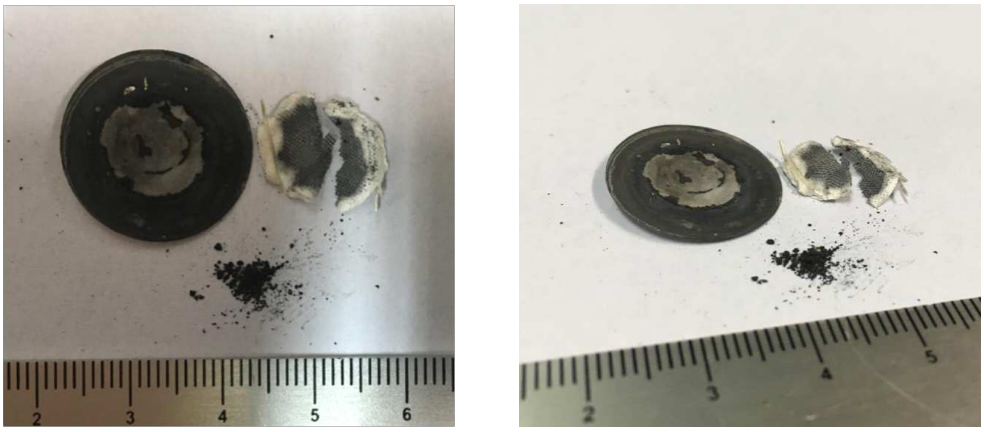

Figure 7. Pictures of the post-mortem anode, right after operation.

Conclusions

This preliminary work, aiming to add copper by wet impregnation, shows the necessity of improving copper distribution throughout the anode bulk. As shown in our previous work, the ceria-Co-Cu anode is promising for ethanol electrochemical oxidation, and it was herein confirmed that copper plays an important role in preventing coking.

The cell was able to operate reasonably with hydrogen delivering 250-300 $mW.cm^{-2}$ of power density at intermediate temperatures such as 750-775°C. The lower performance of the cell with ethanol as fuel was due to the coke formation provoked during operation.

The next steps of this project will be to optimise the anode microstructure and porosity, so that a higher copper load can be accommodated within the anode; improve the impregnation method by performing vacuum impregnation; and improve the ethanol feeding system to avoid condensation throughout the feeding line.

Acknowledgments

The authors would like to acknowledge the financial support granted by FURNAS S.A.

References

1. P. E. V. Miranda, in *Science and Engineering of Hydrogen-Based Energy Technologies* p. 42, Elsevier (2019)
2. L. Troskialina, A. Dhir and R. Steinberger-Wilckens, *ECS Trans*. **68**, 2503 (2015).
3. B. J. M. Sarruf, J-E. Hong, R. Steinberger-Wilckens and P. E. V. de Miranda, *ECS Trans*. **78**, 1343 (2017).
4. E.W. Park, H. Moon, M. Soo Park and S.H. Nyun, *Int J Hydrogen Energy* **34**, 5537 (2009)
5. I. Gavrielatos, V. Drakopoulos, S.G. Neophytides, *J Catal.,* **259**, 75 (2008).
6. A. Coralli, H. V. Miranda, C. F. E. Monteiro, J. F. R. Silva, P. E. V. Miranda, *J. P. Sources*, **269**, 632 (2014).
7. S.A. Venancio and P.E.V. Miranda, *Scripta Materialia* **65**, 1065 (2011).
8. S.A. Venancio and P.E.V. Miranda, *Int J Hydrogen Energy* **42**, 13927 (2017).
9. B. J. M. Sarruf, J-E. Hong, R. Steinberger-Wilckens and P. E. V. de Miranda, *Int J Hydrogen Energy* **43**, 6340 (2018).
10. B. J. M. Sarruf, J-E. Hong, R. Steinberger-Wilckens and P. E. V. de Miranda, *Int J Hydrogen Energy* **In press**, Available online 2 May 2019.
11. ICDD (2016). PDF-4+ 2014 software 4.14.0.6 (PDF-03-065-2975), International Centre for Diffraction Data, Newtown Square, PA, USA.
12. ICDD (2016). PDF-4+ 2014 software 4.14.0.6 (PDF-00-042-1467), International Centre for Diffraction Data, Newtown Square, PA, USA.